Effect of Adsorbate Diffusion on the Dendritic Morphology of Electrodeposited Films

Dung Di Caprio, Abdelhafed Taleb, Fábio Reis

Effect of Adsorbate Diffusion on the Dendritic Morphology of Electrodeposited Films

Dung di Caprio,[*,†] Abdelhafed Taleb,[*,‡] and Fábio D. A. Aarão Reis[*,¶]

†*PSL Research University, Chimie ParisTech - CNRS, Institut de Recherche de Chimie Paris, 75005, Paris, France*

‡*Sorbonne Université, 75005, Paris, France*

¶*Instituto de Física, Universidade Federal Fluminense, Avenida Litorânea s/n, 24210-340 Niterói, RJ, Brazil*

E-mail: dung.di-caprio@chimieparistech.psl.fr; abdelhafed.taleb@upmc.fr; reis@if.uff.br

Abstract

We study the formation of deposits with dendritic morphology using numerical simulations of a model of electrodeposition and diffusion of the adsorbed material. The model considers a diffusive flux of cations in solution, the instantaneous adsorption and reaction in contact with the film surface, and random walks of mobile atoms on that surface, with a maximum of G hops per atom and a detachment probability ϵ per neighbor at the current position. For low temperature or large current, which correspond to small G, the deposits are similar to diffusion-limited aggregates growing from the flat electrode; for high temperature or very small current, which are represented by large G or ϵ, the deposits have thick rounded columns with sporadic ramification. In these conditions, the growth direction is controlled by the orientation of the electrode and of the cation flux. For balanced conditions of adsorbate diffusion and current (typically $10^2 \lesssim G \lesssim 10^4$ and $\epsilon \lesssim 0.1$, but also for larger G and very small ϵ), the films have a hierarchical dendritic morphology with maple leaf shape. The dendrite tips propagate in directions forming 45° with the electrode and are formed by three concurrent terraces, as a consequence of the simulations in a simple cubic lattice. The average dendrite size increases as a power law of G and is consequently expected to decrease with the applied current. The lowest energy configurations (terraces) are shown to be stable within the timescale of crystallization of an atomic layer, but the weakly bonded atoms have sufficiently large mobility to create those configurations. Thus, the dendritic morphology depends on the interplay between the energetics of the crystal and the electric current, which may help the interpretation of dendrite growth with other crystalline structures. The dendrite shape obtained here resembles those observed in some electrodeposited films of gold, zinc, and palladium, and the effect of the electric current on the dendrite size agrees with observations in electrodeposition of silver and gold. Assuming that the adsorbate diffusion is thermally activated, we propose that the average dendrite size is a ratio between an Arrhenius factor and a power law of the current; this suggests a method to estimate the microscopic energy barrier of diffusion, which may differ from the macroscopic activation energy.

1 Introduction

In materials science, there is a widespread interest in developing micro and nanostructured surfaces with controlled morphology and special physical and chemical properties. Among the prepared morphologies, hierarchical structures such as dendrites have attracted much interest due to their potential for technological applications such as self-cleaning,[1–4] sensing,[5] and catalysis.[6] The open porous structure of dendrite morphology provides high surface area in contact with the solvent and the control of wetting, optical, and magnetic behaviors.[7–10]

The electrochemical methods are among the cheapest and most accurate techniques to control the dendrite morphology, which results from a coupling between the applied potential or current with several processes such as ion diffusion in the electrolyte, reaction kinetics, nucleation, and growth on the electrode.[11–15] The sizes and shapes of the dendrites consequently depend on the ion concentration, the physical properties of the electrode, the temperature, and the variations of the electric current. The dendritic films usually have hierarchical configurations with organized micro or nanostructures such as secondary, tertiary, and in some case quaternary subbranches. In works on electrodeposition of copper, silver, and zinc films, the terms leaf-like, feather-like, flower-like, and cauliflower-like were already used to describe dendrite shapes; this reveals the large variety of observed morphologies and suggests a wide range of physical and chemical behaviors. However, depending on the growth conditions, electrodeposited films may also be compact, with low porosity and with relatively smooth surfaces. In other conditions, the films have highly ramified structures with no organization at short lengthscales, which is similar to diffusion-limited aggregation (DLA)[16] or diffusion-limited deposition (DLD).[17–19]

Adsorbate diffusion was shown to be relevant in the initial stages of the electrodeposition of films and nanoparticles[20–24] and for the growth of dendrites.[11,14,25,26] The effects of adsorbate diffusion were also shown in studies of kinetic roughening of compact electrodeposited films.[27–29] Adatom diffusion was considered in a model of instability development in electrodeposition[30] and in kinetic Monte Carlo (KMC) simulations.[31,32]

In a recent work, an electrodeposition model with diffusion of adsorbed atoms was proposed and the formation of a non-porous wetting layer on the electrode was studied.[33] Here we extend the simulations of that model to study the properties of the porous films that grow on the wetting layer, with special interest in the conditions for growth of hierarchically organized structures, i. e. the dendrites. For very low or very high diffusivity of the adsorbate, highly porous or compact branches are formed, respectively; in both cases, they are oriented perpendicularly to the substrate and do not have any special type of internal organization. However, for a certain range of model parameters, we show the formation of dendrites with maple leaf shape. These dendrites are formed by stacking atomic planes which spontaneously grow in various directions, but with a self-organization controlled by the crystallography of the material (i. e. by the lattice structure imposed in the simulations). These features are observed if surface diffusion is facile for weakly bonded atoms, but is severely restricted in low energy configurations, which are effectively stable in the timescale of crystallization of each atomic layer. The results are qualitatively compared with those of electrodeposition of silver, copper, gold, zinc, and palladium; in particular, the results are consistent with the effect of the current on the size of the dendrites of electrodeposited silver and gold. We also propose a method to measure the average dendrite size in the simulated deposits and relate this size to the diffusion length of the adsorbed atoms and, consequently, to the temperature and to the applied current.

The rest of this paper is organized as follows. In Section 2, we define the electrodeposition model and present the interpretation of its parameters. In Section 3, we show the simulation results. In Section 4, we discuss the process of dendrite formation and the dependence of dendrite size on physical parameters. In Section 5, a summary of results and conclusions is presented.

2 Model and methods

2.1 Model definition

The model is defined in a simple cubic lattice because it allows time consuming simulation of very large deposits (this would be much more difficult with other geometries). The lattice constant is taken as the unit length of the model; its value is assumed to be close to the size of an atom, i. e. some tenths of a nanometer. The size of the lattice in x and y directions is L and periodic boundary conditions are considered in those directions to avoid finite-size effects. The working electrode (substrate) is at the plane $z = 0$ and lattice sites with $z > 0$ initially contain a supported electrolyte.

The electrodeposition is modeled as a sequential aggregation of atoms, each one occupying a lattice site. The aggregation of each atom occurs after a sequence of three steps: (i) diffusion of a cation in solution; (ii) adsorption of the cation on the substrate or on the surface of the film, reduction, and formation of a mobile atom; (iii) relaxation by surface diffusion of the mobile atom during a preset time and permanent aggregation of this atom at the final position of this motion.

In step (i), the cation is released at a position $(x, y, h_{max} + 45)$, with randomly chosen x and y, and with h_{max} defined as the maximal value of z of a previously aggregated particle. The cation executes an unbiased random walk (RW) to nearest neighbor (NN) sites in the electrolyte, as illustrated in Fig. 1(a). During this RW, the position z cannot exceed $h_{max}+45$, i. e. the cation is reflected if it reaches that height; this condition is necessary because random walkers in three dimensions have a finite probability of moving forever to regions far from the substrate.[34]

Step (ii) takes place when the cation reaches a site in which at least one NN is an aggregated atom or a substrate site. In Fig. 1(a), this first contact with the deposit is at the site immediately above the yellow atom. At this position, the electrochemical reaction immediately occurs and the reaction product occupies the same site; this product is termed

a mobile atom.

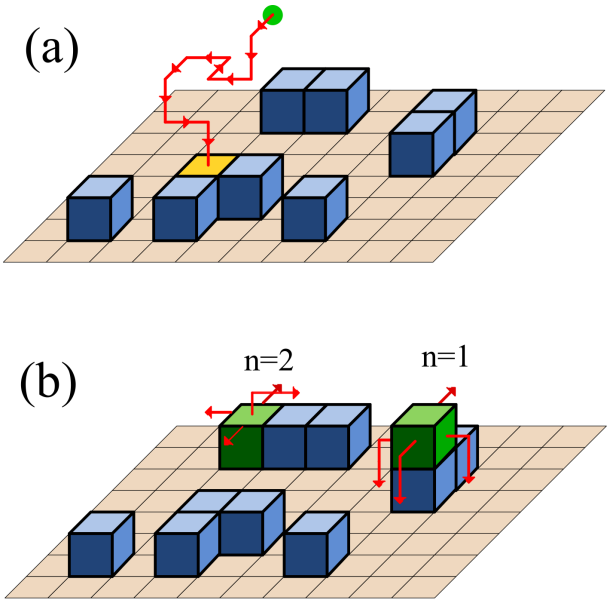

Figure 1: (a) A cation (green circle) in the electrolyte executes a RW whose path is indicated (red line with arrows). The cation stops moving when it reaches a site which has a NN aggregated atom (yellow). Other aggregated atoms are shown in blue color and the substrate is in tan color. (b) Possible hops (red arrows) of two mobile atoms (green), with the respective coordination numbers.

Step (iii) is a RW of the mobile atom, which attempts to execute G hops to NN or to next nearest neighbor (NNN) sites, starting at the position where it was produced. There are two conditions for executing a hop attempt. First, it is possible with probability

$$P_{hop} = \epsilon^{n-1}, \tag{1}$$

where n is the number of occupied NN of that position (i. e. NN aggregated atoms plus NN substrate sites) and ϵ is termed the detachment probability per NN. Second, a target site is randomly chosen among the NN and NNN sites of the current position and this target site has to be empty and has to have at least one occupied NN. If some of these conditions is not satisfied, the hop attempt is rejected and the mobile atom remains at the current position. The first condition means that the mobility of the atom is lower (higher) at points with higher (lower) coordination. The condition that the target site has at least one occupied NN

means that desorption is not allowed. Fig. 1(b) shows the directions of the possible hops of two mobile atoms in a deposit [note that only one mobile atom is at the surface at each time, thus two mobile atoms are shown in Fig. 1(b) only for the sake of illustration].

2.2 Simulation method

Simulations of the model were performed in lattices with $L = 1536$ until the maximal height reached the value $h_{max} = 1480$ (in lattice units). Several values of G from 20 to 10^4 were considered, as well as the DLA case ($G = 0$). The values of ϵ were between 0.02 and 0.25.

For several set of parameters with $20 \leq G \leq 10^4$, 100 different deposits were grown, which allows the calculation of accurate distributions of dendrite size. The number of deposits was 10-20 for $G = 5 \times 10^4$ and several values of ϵ because simulation of large values of G consume a long time, which can amount to weeks for a single deposit. For other parameter sets, a few deposits were grown because they aimed only at distinguishing the type of morphology (namely, dendritic or not).

Simulations were run on Nvidia Tesla K80 graphic cards in the CUDA environment for parallelization. In a simulation step, a total of 2496 cations is simultaneously released above the film, corresponding to the number of processors. In this parallel process, more than one mobile atom may reach the same final site due to the slow update of the memory, which does not signal that site as being already occupied. This case is more frequent when ϵ is small and at sites with a large number of neighbours, in which the residence time of a mobile atom is large. In such case, the actual number of deposited particles is counted and the missing number due to multiple particles on the same site is added by performing supplementary depositions.

2.3 Interpretation of the model

Step (i) represents the movement of cations in a supported electrolyte, where the electric field is shielded by a high concentration of inactive ions.[35] The use of lattice RWs to simulate

the motion of the cations is also justified by their small mean free path in solution, even when there is a depleted layer above the growing film.

Step (ii) represents two processes which are assumed to have very high rates (due e. g. to negligible energy barriers): the adsorption of the cation and the electrochemical reaction. For this reason, when the cation reaches the film surface, those processes are modeled as an instantaneous transformation of a cation into a mobile atom. Steps (i) and (ii) form the set of rules of the DLD model, in which the reaction product is immediately aggregated at the point of adsorption ($G = 0$).[17,18]

Step (iii) is a simplified description of the effects of adsorbate diffusion. The number of hop attempts of a mobile atom, G, is expected to be proportional to the time of diffusion of the atom before it is incorporated to the growing crystal. If the temperature increases, the diffusion coefficient of such atom increases, then the relaxation to longer distances is possible. Moreover, if a single electrochemical reaction occurs, the rate of cation reduction is proportional to the current, and so is the rate of crystallization (which is the deposition rate); the increase of the current then leads to a decrease in the relaxation time before crystallization. Thus, the increase of temperature or the decrease of the current is represented by an increase of G in the model.

Note that the present model is of limited mobility, since the aggregation position of an atom is chosen before the incidence of another atom. This is the reason for a finite number of hop attempts. Instead, in collective diffusion models, there is simultaneous particle flux and diffusion of all atoms at the surface of the deposit; in this case, there is no constraint for the diffusion time (or diffusion length) of an adatom. However, any adatom is expected to reach a final aggregation position during the film growth because it will be buried below some crystalline layers. This means that it executes a finite number of hops at the film surface. The algorithm with a sequential aggregation of atoms (limited mobility) is an approximation that allows the simulation of larger systems.

The probability P_{hop} for the mobile atom to hop to a neighboring point represents the

effects of the local surface morphology on the atom mobility. $P_{hop} = 1$ for the mobile atom on a terrace, since the number of neighbors in the crystalline phase is small ($n = 1$); otherwise, $P_{hop} < 1$. If $\epsilon \ll 1$, then the atoms with high coordination have very low mobility.

In electrodeposition, the adsorbate diffusion may be quite complicated and is very different from the adatom diffusion in metal surfaces growing from vapor. For instance, in silver electrodeposition, it was shown that dendrites grow with the formation of an amorphous phase ($\sim$ 5nm thick) at their tips and the subsequent crystallization of that phase.[25] Molecular dynamics simulations suggest that water absorption is responsible for maintaining the amorphous phase.[36] In lead electrodeposition, polycrystalline nanograins are formed in the dendrite tips, but subsequent alignment and aggregation leads to formation of a single crystal and the propagation or splitting of the dendrite.[37] Our model assumes that the adatom mobility in those amorphous or polycrystalline phases is controlled by the parameter G, while the preferential crystallization at points with high coordination is mainly controlled by the parameter ϵ.

For the parameter ϵ in Eq. (1), a thermally activated form may be proposed as

$$\epsilon = \exp\left(-E_b/k_B T\right), \tag{2}$$

where $E_b > 0$ is the activation energy and T is the temperature. For low temperatures or large E_b, P_{hop} is very small at points where many neighbors are in the crystalline phase (e. g. $n = 3$ or larger). For high T or small E_b, P_{hop} slowly varies with the coordination number n.

It is important to observe that both G and ϵ increase as the temperature increases. For this reason, the results in which only one of those parameters vary cannot represent effects of varying the temperature. Since only G is expected to depend on the applied current, the qualitative effects of current variations may be interpreted by varying only this parameter.

Note that several works classify electrodeposition processes as diffusion-controlled or

reaction-controlled, but this is not applicable to the present model. That classification is possible in systems where the reaction rate varies and where it competes with ion diffusion in the electrolyte to control the film morphology. For instance, the interplay of these processes in the electrodeposition of silver particles was recently discussed.[15,38] However, our model always represents processes with high reaction rate and considers a third process, viz. diffusion of the adsorbate.

3 Results

3.1 Film morphology for small G and ϵ

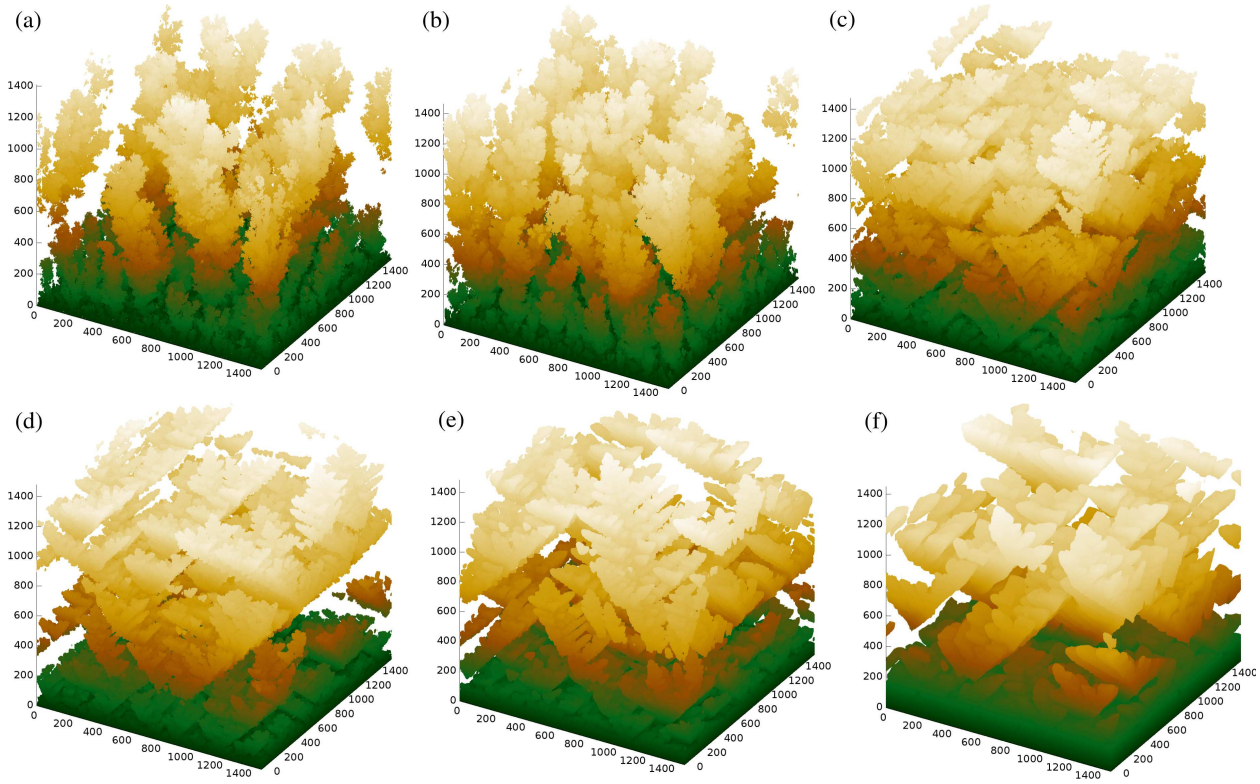

Figure 2: Images of deposits grown with G = (a) 0, (b) 20, (c) 100, (d) 500, (e) 2×10^3, (f) 10^4. In all cases, $\epsilon = 0.05$.

Figs. 2(a)-(f) show images of films grown with several values of G and $\epsilon = 0.05$. Figs. 3(a)-(f) show the corresponding top views of those films and Figs. 4(a)-(f) show the lateral views.

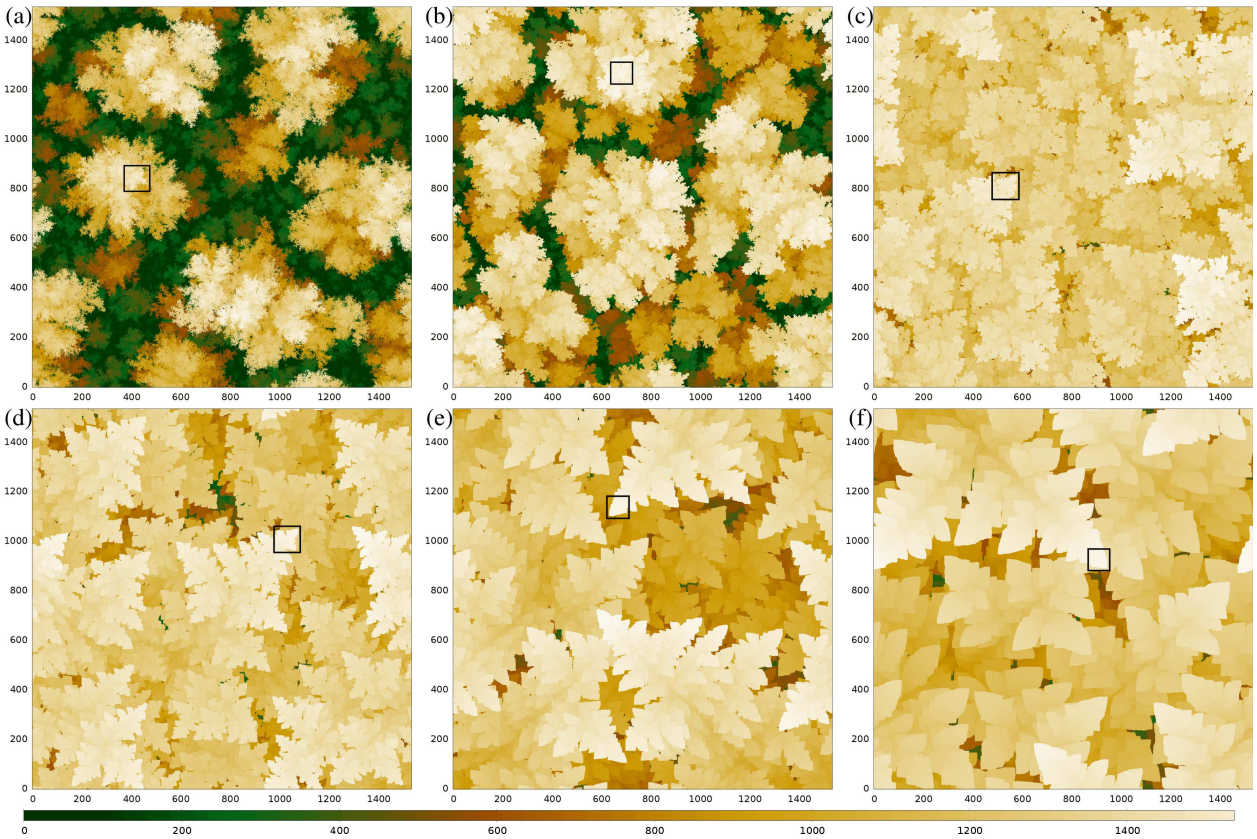

Figure 3: Top view of deposits grown with parameters as in Fig. 2: G = (a) 0, (b) 20, (c) 100, (d) 500, (e) 2×10^3, (f) 10^4. In all cases, $\epsilon = 0.05$.

For $G = 0$ (DLD model[17,18]), branches of different sizes and heights grow vertically from the electrode with frequent lateral ramification. Due to the stochastic nature of the flux, some branches grow faster than the others, which are shadowed and stop growing. For this reason, a small number of branches reach the largest heights of the simulation cell [those with brighter colors in Fig. 3(a)]. For $G = 20$ [Fig. 3(b)], the deposits are also similar to those of DLD, with thin branches growing vertically from the substrate and splitting several times. The top branches are wider than those of DLD, since the mobility of adsorbed atoms facilitates lateral ramification.

For $G = 100$ and $\epsilon \leq 0.1$, the film morphology is very different from DLD. Instead of the random orientations of the branches observed for $G \leq 20$, the top view in Figs. 3(c) ($G = 100$) shows the formation of organized structures with the shape of maple leaves. This type of hierarchical structure is simply called dendrite in the rest of this work. Figs. 2(c)

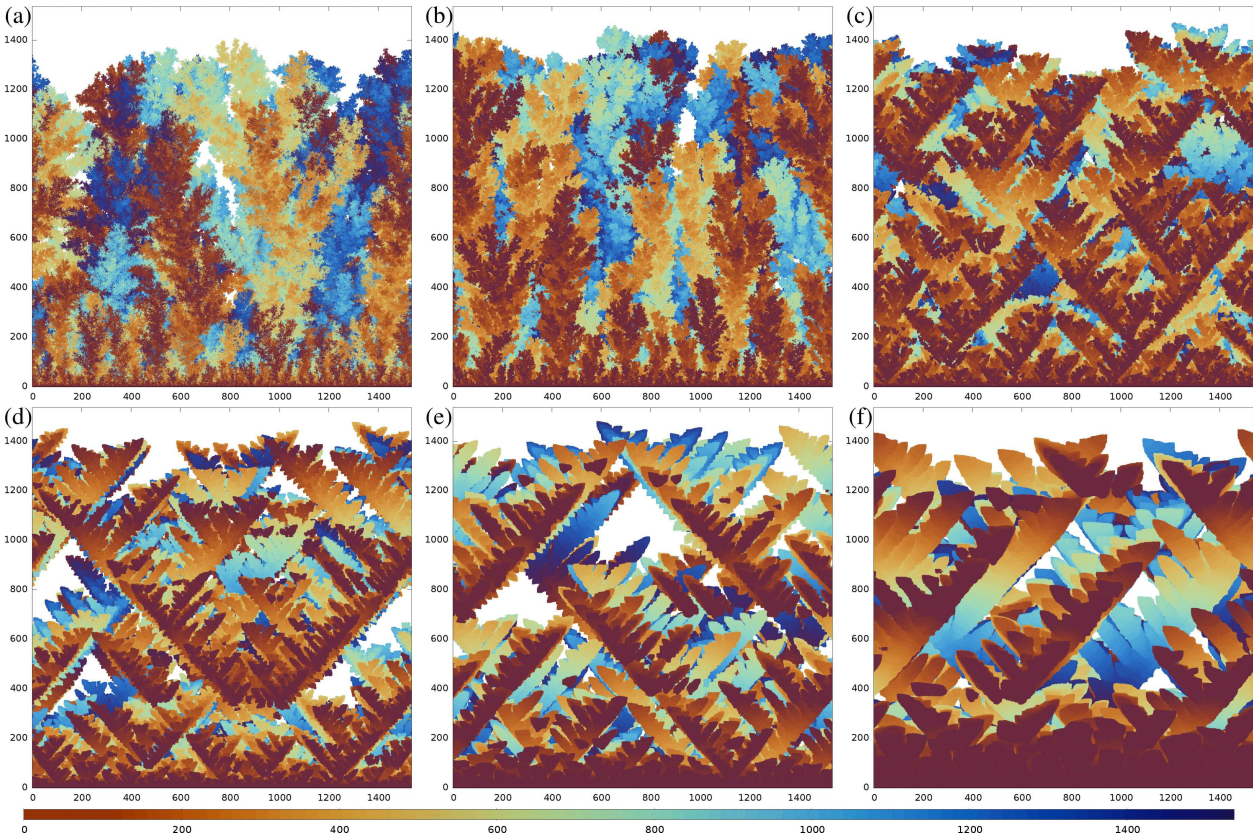

Figure 4: Lateral view of deposits grown with parameters as in Fig. 2: G = (a) 0, (b) 20, (c) 100, (d) 500, (e) 2×10^3, (f) 10^4. In all cases, $\epsilon = 0.05$.

and 4(c) show that the dendrite tips may grow in four directions, $(\pm 1, \pm 1, 1)$, i. e. they form angles of 45° with the z axis. This also contrasts with the dominant vertical orientation of the branches in the growth with $G \leq 20$ [Figs. 2(a),(b) and 4(a)-(b)]. When a branch of a dendrite splits, the sub-branches grow in one or more of those four directions.

For $G > 100$, the growth of leaf-shaped dendrites in directions $(\pm 1, \pm 1, 1)$ is also observed for several values of ϵ. The average size of the leaves increases with G; see Figs. 2(c)-(f), 3(c)-(f), and 4(c)-(f).

Figs. 5(a)-(f) show magnified views of the regions indicated by square boxes in the top views of Figs. 3(a)-(f). For $G \leq 20$, there is only random growth and ramification; no organized structure is formed, even in very small lengthscales. Some degree of organization is observed for $G = 100$, with small terraces formed at the top of the dendrites. For $G \geq 500$, we distinctly observe nontrivial structures in the leaf-like dendrites, which are formed by

stacked horizontal terraces.

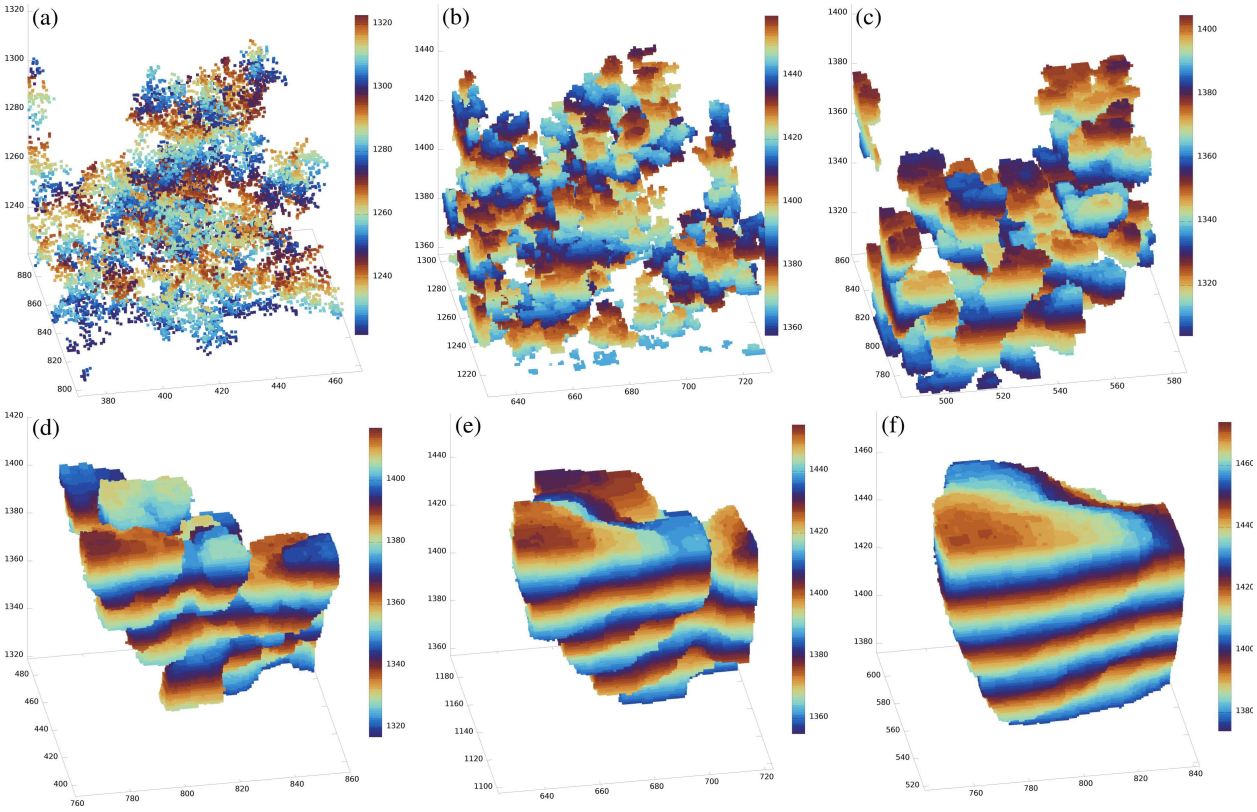

Figure 5: Side views of $100 \times 100 \times 100$ size boxes of the areas indicated in Figs. 3(a)-(f): $G =$ (a) 0, (b) 20, (c) 100, (d) 500, (e) 2×10^3, (f) 10^4. Cyclic palette is used to help visualization of horizontal terraces.

For other small values of ϵ, the film morphology is similar to that for $\epsilon = 0.05$. This is shown in the images of Figs. 6(a) and 6(b) for $(G = 500, \epsilon = 0.02)$ and $\left(G = 10^4, \epsilon = 0.1\right)$, respectively. The leaf-like dendrites thicken as ϵ increases, but this is a relatively small effect. For instance, as ϵ changes by a factor 5 (from 0.02 to 0.1), the dendrite thickness increases $\sim$ 20-30%, while a change of G by a factor 5 leads to an increase in the thickness by a factor larger than 3. These effects are quantitatively described in Sec. 3.4.

At dendrite tips, we observe that three concurrent and perpendicular terraces intersect. The top terraces are visible in Figs. 5(d)-(f), which also show the nucleation of new terraces on them. Figs. 7(a)-(c) show magnified lateral views of the regions indicated in Figs. 4(d)-(f), respectively, and confirm the presence of the lateral terraces at the dendrite tips. Two

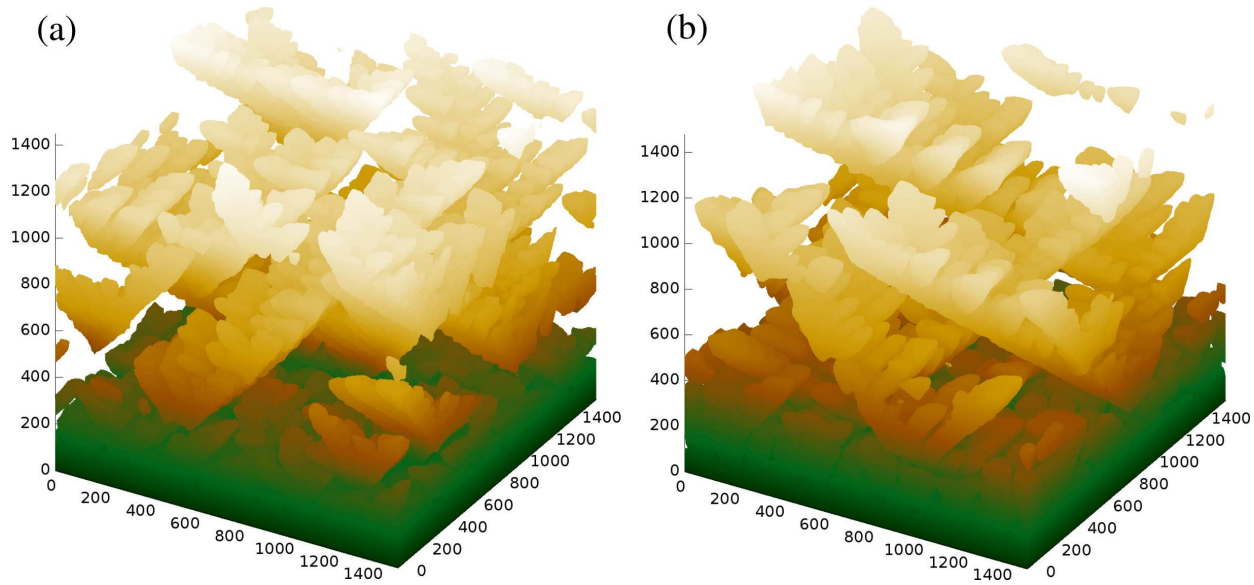

Figure 6: Images of deposits grown with (a) $G = 500$, $\epsilon = 0.02$, and (b) $G = 10^4$, $\epsilon = 0.1$.

movies in the Supporting Information show top and lateral views of the growth of a dendrite tip and also confirm these observations.

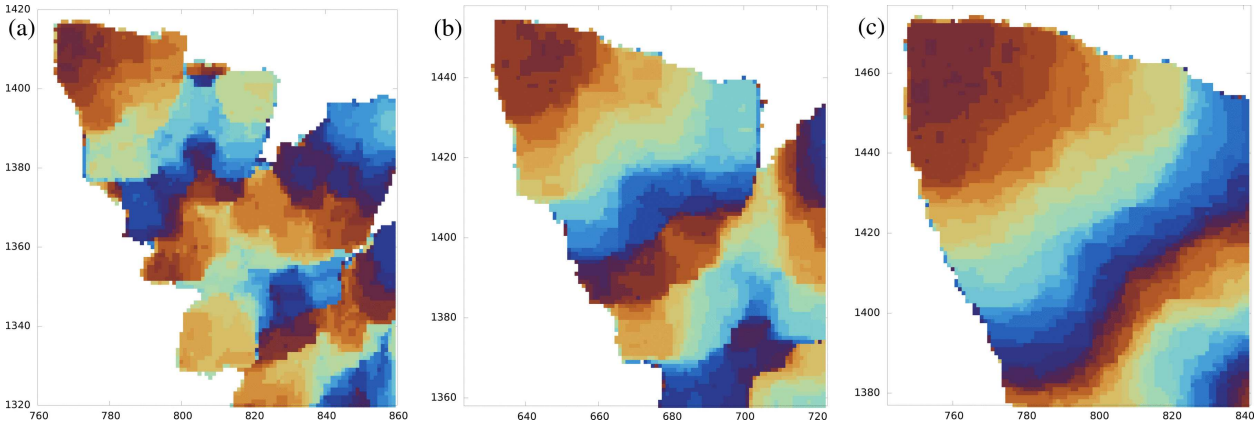

Figure 7: (a), (b), and (c) show lateral views of the dendrite tips shown in Figs. 5(d), (e), and (f), respectively.

3.2 Small interaction regime

Here we analyze the simulation results for very large G and $\epsilon = 0.25$. The large values of ϵ are expected to represent deposition in high temperatures or with small bond energy E_b; see Eq. (2). Large values of G correspond to high temperatures or to very small applied current.

If G has thermally activated form, then large G may also correspond to small bond energy of atoms on terraces. Thus, a variety of physical and chemical conditions may be associated to large G and large ϵ, but all them are consistent with large mobility of the adsorbed atoms; this justifies the term small interaction regime.

First consider the film morphology for $G = 5 \times 10^4$ and four values of ϵ, as shown in Fig. 8. In all cases, we observe a thick wetting layer on the electrode, as shown in Ref. 33. For $\epsilon \leq 0.05$, dendrites with leaf like shape are formed and propagate in $(\pm 1, \pm 1, 1)$ directions, as occurred for smaller G. However, for $\epsilon \geq 0.1$, thick rounded columns grow vertically above the wetting layer, with sporadic ramification.

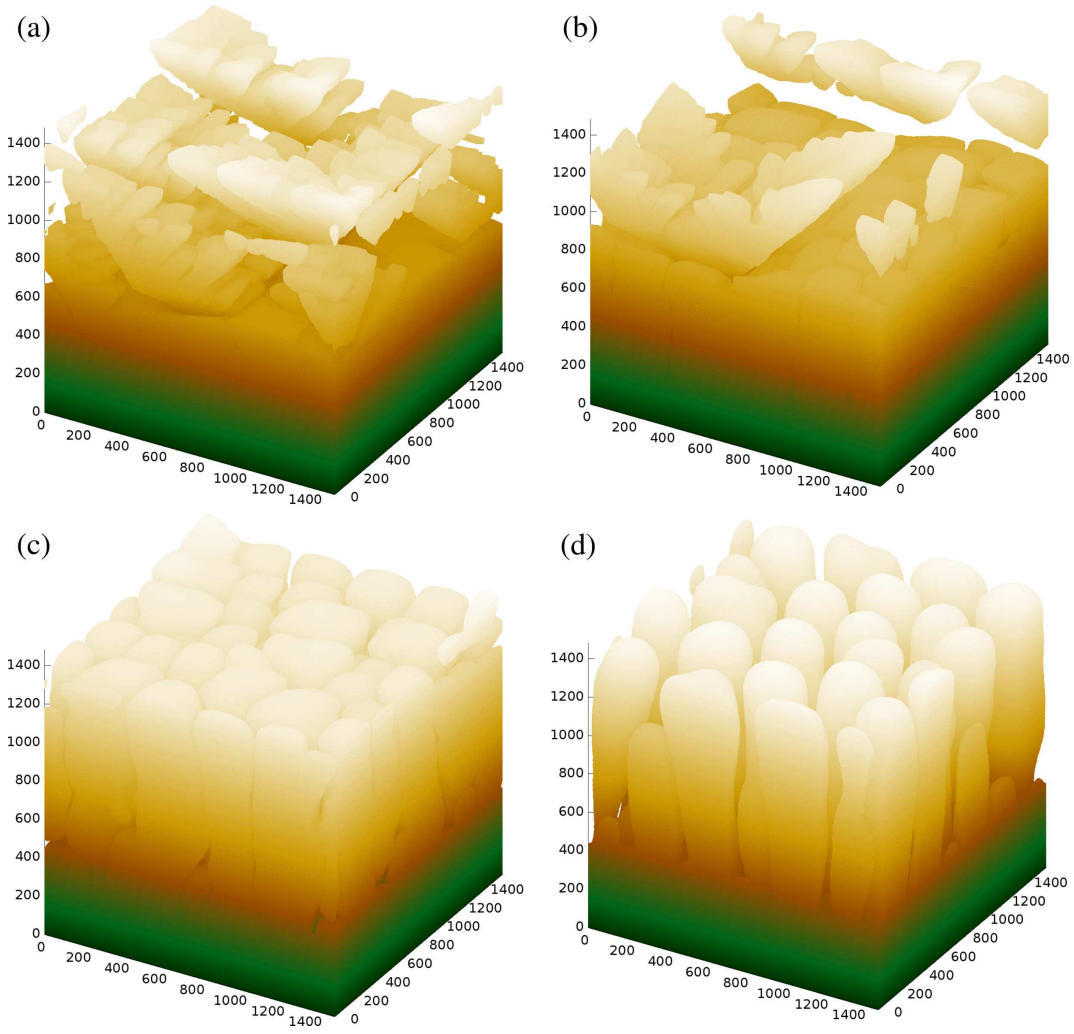

Figure 8: Deposits grown with $G = 5 \times 10^4$ and $\epsilon =$ (a) 0.02, (b) 0.05, (c) 0.1, and (d) 0.25.

Now consider the case $\epsilon = 0.25$ and $G \geq 500$. Figs. 9(a)-(c) show images of deposits grown with three values of G and Figs. 9(d)-(f) show the top views of the same deposits. Figs. 9(g)-(i) show magnified views of the regions indicated with square boxes in Figs. 9(d)-(f); note that the views in Figs. 9(g)-(i) are in three-dimensional perspective. There is no formation of leaf-like dendrites in these cases and the orientation of the branches is predominantly vertical. The bifurcation of the branches are very rare for large G. The top parts of those branches have stacked horizontal terraces, but they have rounded edges. This contrasts with the shape with three concurrent terraces (sharp edges) observed for small ϵ.

3.3 The range of parameters with dendrite growth

Fig. 10 shows the type of morphology observed for each simulated value of G and ϵ. That diagram distinguishes three cases: (i) the regime in which dendrites are formed immediately above the compact wetting layer; as defined above, the term dendrite is used here only for the structures with maple leaf shape propagating in $(\pm 1, \pm 1, 1)$ directions; (ii) the cases in which the branches predominantly grow in the vertical direction with no internal organization; this may include thin branches with many ramifications (DLD-like shape) or thick branches with rare ramification; (iii) the transition cases in which the previous features coexist in the simulation cell. A smaller number of data points is presented for $G = 5 \times 10^4$ because the simulations are very long in this case.

In the range $10^2 \leq G \leq 2 \times 10^4$, the dendrites are observed for all $\epsilon \leq 0.1$ and possibly for some larger values of ϵ. For much smaller or much larger G, the dendrites are formed only for small ϵ. In Fig. 10, the upper bound of the dendrite region (i. e. the set with the largest ϵ for each G) is not symmetric; thus we did not find any simple relation bewteen G and ϵ to characterize that region.

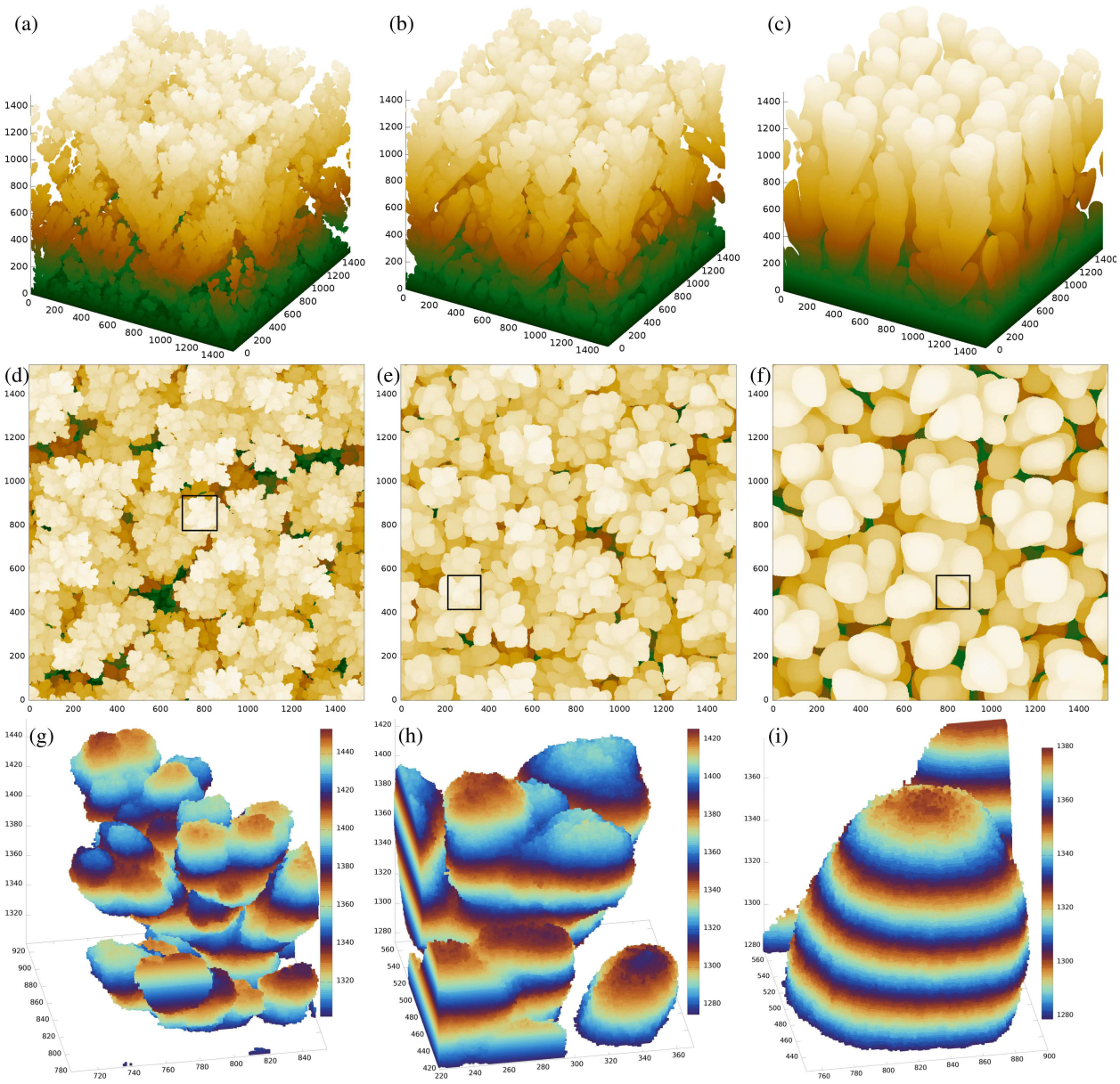

Figure 9: Deposits grown with $\epsilon = 0.25$. (a), (d), (g): side view, top view, and detail of the region indicated in the top view, respectively, for $G = 500$; (b), (e), (h): side view, top view, and detail, respectively, for $G = 2 \times 10^3$; (c), (f), (i): side view, top view, and detail, respectively, for $G = 10^4$.

3.4 The size of the dendrites

There are four possible orientations of dendrites in our simulations and their sizes and locations change in different realizations. As a dendrite splits, it is difficult to define precisely which atoms belong to the primary or to the secondary one. For these reasons, the distri-

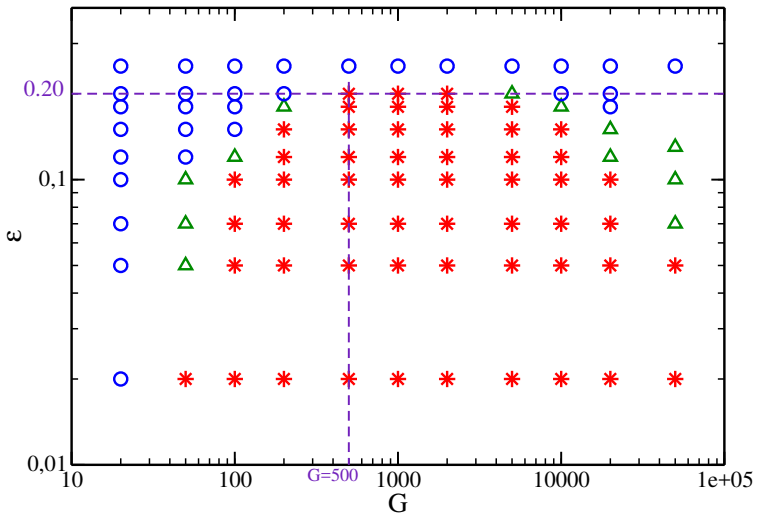

Figure 10: Film morphology as a function of G and ϵ, with red stars indicating dendrites with maple leaf shape propagating in $(\pm 1, \pm 1, 1)$ directions, blue circles indicating thin or thick branches with vertical alignment, and green triangles indicating transient structures. Dashed lines are provided as guide to the eye.

bution of dendrite size (or dendrite thickness) has to be measured with some approximation procedure.

All dendrites propagate in some direction with a vertical (z) component. Thus, the size of a horizontal cross section of a dendrite (i. e. a section with constant z) is of the same order of magnitude as the size of a cross section in a plane perpendicular to the propagation direction. Since this direction forms 45° with the z axis, the two cross sections differ by a factor $\sqrt{2}$. In order to measure the sizes of the horizontal cross sections, we slice the deposit in planes with fixed z (i. e. parallel to the substrate) and, in each slice, we enumerate the clusters of NN connected atoms and calculate the number of atoms (size) s of each cluster. The identification of connected clusters is done with the Hoshen-Kopelman algorithm with periodic boundaries in the horizontal plane.[39] The slices are taken only at heights in which the porosity reaches a height-independent value; some plots of film density were provided in Ref. 33. The size distributions obtained with this procedure are termed dendrite size distributions, although we understand that the enhancement factor $\sqrt{2}$ is present.

Figs. 11(a)-(f) show slices taken from deposits grown with the same parameters as in

Fig. 2(a)-(f) at a height $z = 900$; different colors distinguish different islands. Those images confirm that dendrites with leaf shape are visible for $G \geq 100$ and thicken as G increases. They also show that the leaves are oriented along the 45° directions in the horizontal plane. Due to the tree-like structure of the deposit, some of the clusters in these cross sections represent areas of branch bifurcation and have sizes much larger than the average.

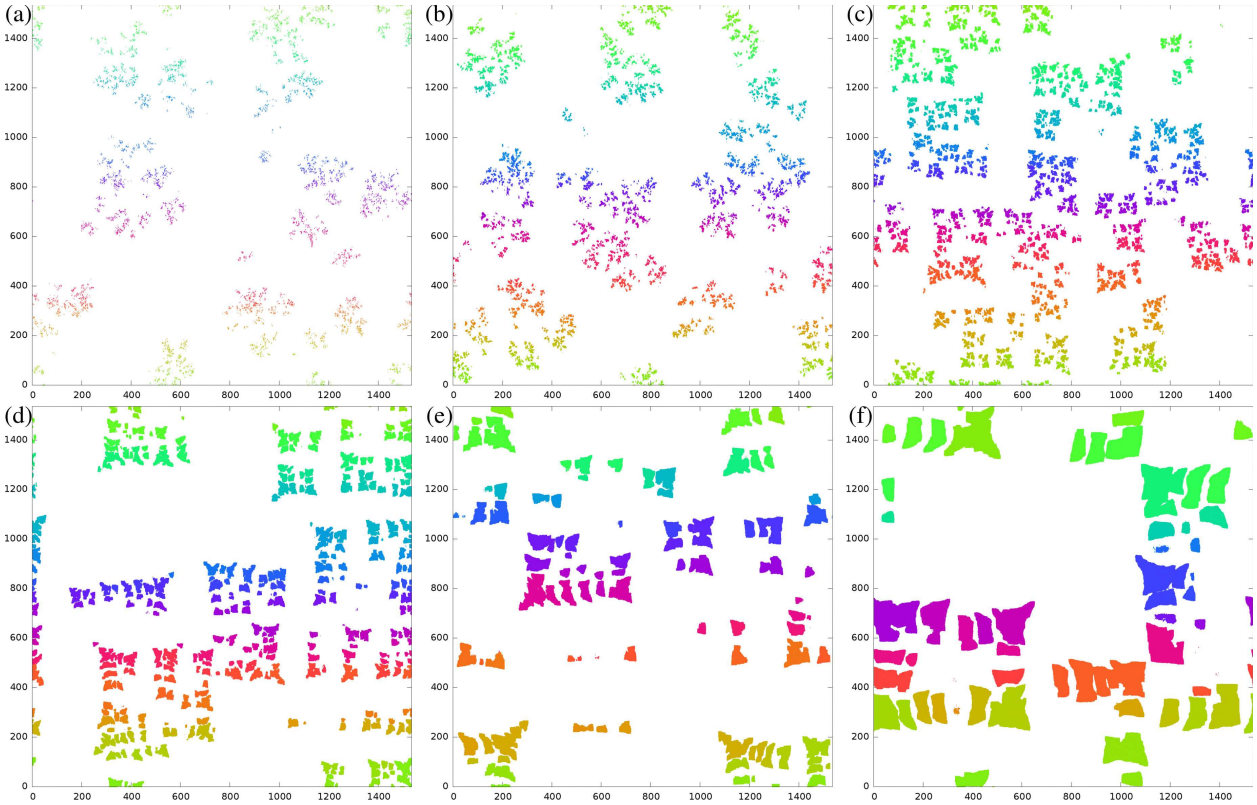

Figure 11: Horizontal slices at height $z = 900$ of deposits grown with parameters as in Fig. 2: $G =$ (a) 0, (b) 20, (c) 100, (d) 500, (e) 2×10^3, (f) 10^4. In all cases, $\epsilon = 0.05$.

In Figs. 12(a)-(f), dendrite size distributions are shown for the same parameter values of Figs. 2(a)-(f). In DLD ($G = 0$), the distribution is peaked at $s = 1$, due to the large number of threadlike branches, and rapidly decreases for $s > 1$. For $G = 20$, there is a peak at $s > 1$, but the most probable size is also $s = 1$; the thickening of some branches is not sufficient to organize their structure. For $G \geq 100$, a peak at a position $s_M \gg 1$ is observed and s_M rapidly increases with G. For $G \geq 2000$, we also observe the gradual formation of a shoulder at a size $\sim 2s_M$; this shoulder appears because the masses of two secondary dendrites (near

a point of splitting of the primary branch) may collapse into a single cluster in the sliced deposit.

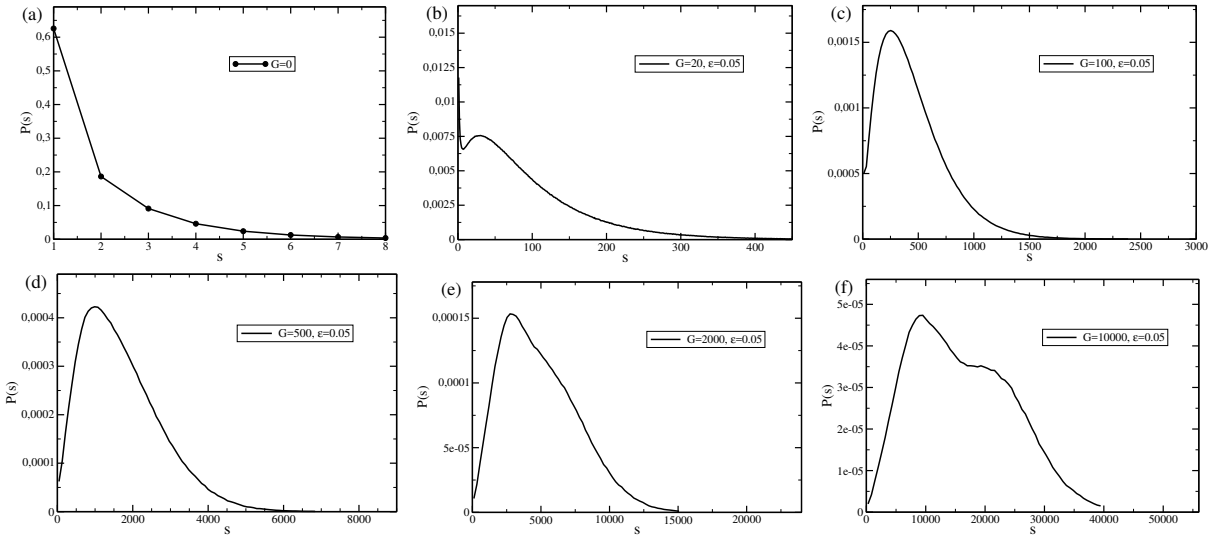

Figure 12: Dendrite size distributions $P(s)$ obtained from horizontal slices of deposits grown with parameters as in Fig. 2: $G =$ (a) 0, (b) 20, (c) 100, (d) 500, (e) 2×10^3, (f) 10^4; in all cases, $\epsilon = 0.05$.

In Figs. 13(a) and 13(b), we show the dendrite size distributions for $G = 500$ and $G = 10^4$, respectively, in both cases with three values of ϵ. Small values of ϵ (up to 0.05) weakly affect the distributions, but a significant broadening is observed for $\epsilon = 0.1$. For $G = 10^4$, the shoulder at $s \sim 2s_M$ is observed for all values of ϵ.

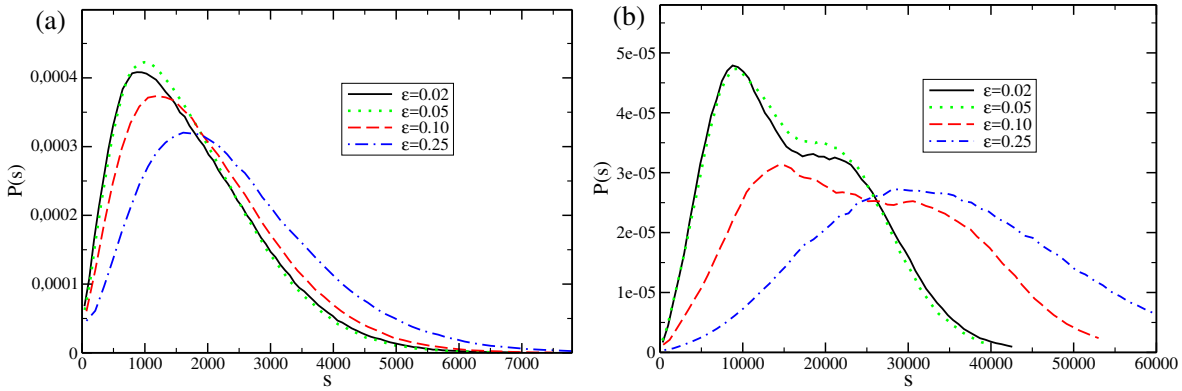

Figure 13: Dendrite size distributions $P(s)$ obtained from horizontal slices of deposits grown with (a) $G = 500$ and (b) $G = 10^4$, for values ϵ as indicated.

Fig. 14 shows the average dendrite size $\langle s \rangle$ as a function of G for the values of $\epsilon \leq 0.1$

considered here. $\langle s \rangle$ has a significant variation with G, but weakly depends on ϵ. Fits of the data for constant ϵ and the largest values of G are also shown in Fig. 14; they are consistent with power law relations

$$\langle s \rangle \sim G^{\alpha}. \tag{3}$$

For the smallest ϵ, we obtain α between 0.76 and 0.78. For $\epsilon = 0.1$, a larger α is obtained.

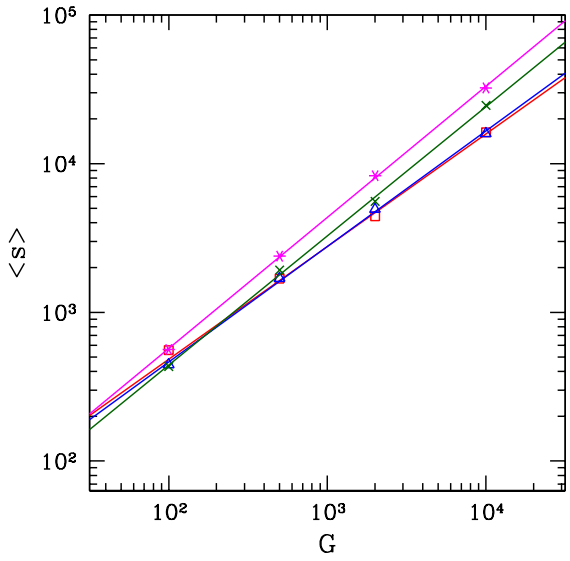

Figure 14: Average dendrite size as a function of G for $\epsilon = 0.02$ (red squares), $\epsilon = 0.05$ (blue triangles), $\epsilon = 0.1$ (green crosses). Dashed lines are least squares fits of the data for fixed ϵ, with slopes 0.75, 0.78, and 0.86, respectively.

4 Discussion

4.1 Comparison with the morphology of electrodeposited films

The dendrite shapes observed here resemble those observed in the electrodeposition of metals by several authors. Flower-like gold nanostructures were obtained in deposition in positive potential on indium tin oxide (ITO) electrode[40] and in cyclic voltammetry on ITO surface

funcionalized with a biopolymer.[41] Similar shapes were observed in electrodeposition of zinc and cobalt,[42–44] with formation of stacked layers in zinc dendrite leaves.[42] Nanostructures with flower shape were also shown in electrodeposited palladium films.[45] Despite the simplifications of our model, this comparison shows that the film morphology obtained here is realistic for some materials in certain growth conditions.

The film morphology in the small interaction limit is consistent with that of copper and zinc electrodeposits:[46–48] at short times, thick layers were formed on the electrode; at long times, thick branches with a small number of ramifications points grew above those layers. In those works, the growth was performed near room temperature, but they took several hours, which suggests that the deposited atoms had long times to move at the film surface. Recently, Ref. 49 showed the formation of a compact layer before the growth of thick branched structures in cooper electrodeposition; in this case, the timescales were much smaller ($\sim$ 1s), but the applied current was also very small. In a study of the early stages of copper electrodeposition, it was shown that the layer formed on the substrate has large crystalline domains, but dendrites are subsequently formed by much smaller crystals.[14] This is also consistent with the observations of our model, in which the compact layer represents the initial large crystals.

4.2 Microscopic processes in the dendrite growth

Fig. 15 shows a simplified scheme of a dendrite tip with three concurrent terraces and illustrates some elementary steps that contribute to the morphology, propagation, and ramification of this dendrite.

A mobile atom on a terrace can move freely on its surface because $P_{hop} = 1$ ($n = 1$). However, for the formation of a terrace, the mobile atoms with low coordination ($n = 1$ and 2) have to migrate to long distances and aggregate at the terrace borders; thus, G has to be sufficiently large. Since hops to NNN sites are possible, the hops between two perpendicular terraces occur without energy barriers; see Fig. 15(a). This means that the three terraces at

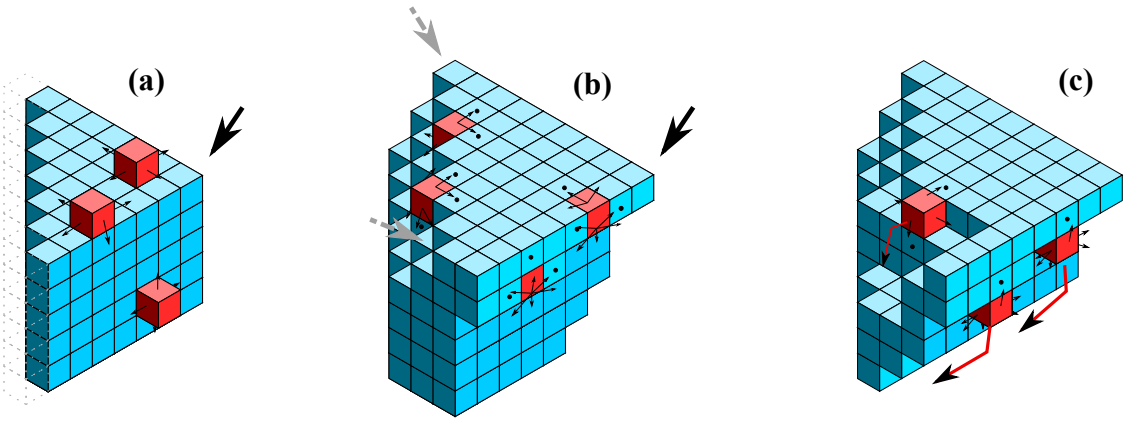

Figure 15: (a) Terraces formed at the tip of a dendrite propagating in $(1, 1, 1)$ direction. (b) Stable edges and possible hops of particles with 3 or more NNs. (c) Mobile particles with 2 NNs. Red cubes indicate moving cubes with arrows pointing in possible directions of movement. Bullet symbol indicates (NN) cubes interacting with the moving red cube. Red arrows show average movement of more mobile particles. Black and grey arrows indicate main and secondary directions of aggregating particle flux.

the dendrite tip are almost equivalent to a single terrace for the atom diffusion.

If $G \sim 10^2$-10^3 and ϵ is small, the atoms in the terrace borders are almost stable. For instance, if one of the terrace atoms is mobile, it will have 3 or 4 occupied NN; $n = 3$ at the tip vertex and at kink sites, $n = 4$ at flat terrace edges. In growth with $\epsilon = 0.02$-0.1, the motion of a mobile atom with $n = 3$ requires at least 10^2-2.5×10^3 hop attempts, and the motion with $n = 4$ requires at least 10^3-1.25×10^5 attempts. Here, we use the term "at least" because, in each hop attempt, there are 18 possible target sites (NN and NNN), but the hop is executed only if the target site is empty and has an occupied NN; see Fig. 1(b). Thus, when the mobile atom reaches a position with 3 or 4 NN, it will probably not move anymore.

Since the cations are released at heights well above the topmost point of the deposit, most of them are adorbed/reduced at the top terrace of the dendrite or at the lateral terraces. When the existing terraces are sufficiently large, the mobile atoms cannot reach their borders and nucleate new islands, which leads to the propagation of the dendrite [the new layer extends at least one site further than the original plane, as shown in Fig. 15(b)]. The mobile atoms in the ridge are in almost stable positions when they reach the borders of the new

terraces; see e. g. the red atoms in Fig. 15(b). This leads to the staircase morphology visible in the simulations; Figs. 5(d)-(f). Fig. 15(c) highlights atoms with $n = 2$ when a new layer is being formed. If they are mobile atoms, they may move up and contribute to formation of the terrace at the top, but they may also move down and contribute to nucleation of lateral terraces, consequently leading to the global thickening of the branch.

The black arrow in Fig. 15(b) indicates the direction $(1, 1, 1)$ of propagation of the dendrite. The stability of atoms in the regions indicated by gray arrows and the production of other mobile atoms at the top terrace lead to formation of secondary branches, which can propagate in directions perpendicular to $(1, 1, 1)$: $(-1, 1, 1)$ and $(1, -1, 1)$, i. e. with a change in the sign of only one component (x or y). In all cases, the slopes of the secondary branches are also 45° respectively to the substrate, as observed in Figs. 4(c)-(f).

The relative stability of growing terraces may be quantitatively explained by comparing the waiting times of the mobile atoms in each neighborhood with their total time of surface diffusion. The average number of hop attempts for an adatom to move from a site with n neighbors is of order ${P_{hop}}^{-1} = \epsilon^{-(n-1)}$; this may be viewed as the waiting time for detachment from a given neighborhood. The ratio between the number of hop attempts G and this waiting time is

$$r_n \equiv G\epsilon^{(n-1)}. \tag{4}$$

If this ratio is large, then the detached atom probably has a large mobility; if this ratio is ~ 1 or smaller, the detachment is unlikely. Fig. 16 shows the values of r_n with $n = 1 \ldots 5$ for points in the upper boundary of the dendrite region of Fig. 10. In other points of the dendrite region, the values of r_n are smaller.

For $G \sim 10^2$, after a detachment event, the number of remaining hops of the mobile atom is probably small. This increases the disorder at the film surface because the atom cannot migrate to high coordination sites. For this reason, the organization of the dendrite structure requires small detachment probability ϵ; note the very small values of r_n for $n \geq 3$ in Fig. 16.

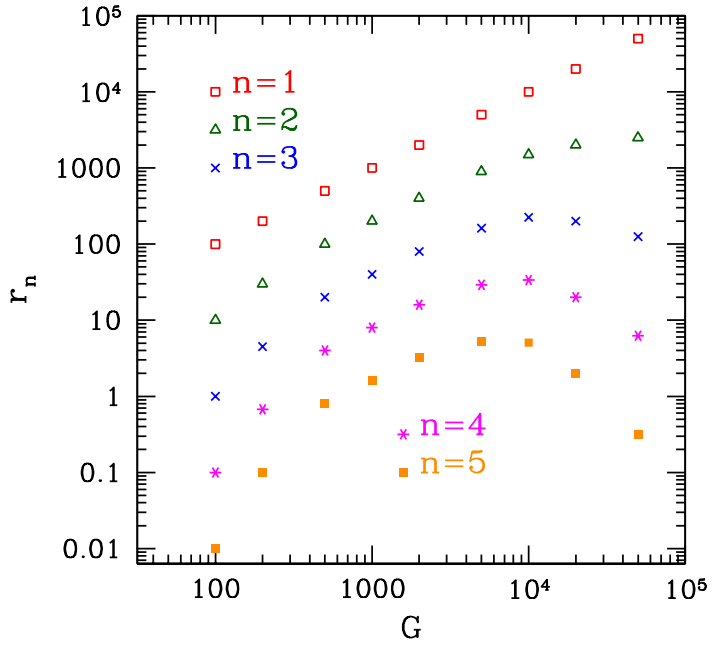

Figure 16: The ratio r_n between the number of hop attempts and the waiting time with n neighbors as a function of G for three different neighborhoods in the upper boundary of the dendrite region.

For $G \sim 10^3$-10^4 and relatively large ϵ, the motion of atoms with $n = 3$ or $n = 4$ is much more probable; see Fig. 16. However, after a detachment event, the mobile atom can still execute a large number of hops because G is large; thus, the detached atom can move to another point with high coordination. Anyway, note that terrace edge detachment ($n = 4$) is not frequent because $G\epsilon^3 \lesssim 30$ for all cases in the dendrite region; Fig. 16.

For $G > 10^4$, large values of ϵ also have a disordering effect because atoms can frequently move from high coordination sites; thus, the configurations with three concurrent terraces become unstable. For this reason, dendrites are observed only for small ϵ. The data in Fig. 16 shows that atoms with $n = 4$ (flat terrace edges) are effectively stable and atoms with $n = 3$ (kink sites) have very low mobility.

4.3 The conditions for dendrite growth

When surface diffusion is negligible (very small G), branched films grow from the substrate and no wetting layer is formed. These films have the same structureless shape of the deposits grown with DLD ($G = 0$). The only noticeable difference is the increase in the lateral size of the branches; see images for $G = 20$ in Figs. 2(b), 3(b), and 4(b). In all cases, the growth direction is controlled by the orientation of the substrate and of the plane where cations are released (the top of the simulation cell). The spread of the branches is isotropic in the x and y directions and is a consequence of the propagation of correlations, as expected in any kinetic roughening process.[50]

For $G \sim 100$ and $\epsilon \leq 0.1$, surface diffusion begins to play an important role. The dendrites have organized structure, in contrast with the randomly growing branches obtained for small G. The diffusion length of the weakly bonded atoms ($n = 1$ and 2) is significantly larger than the average interatomic distance, which is the unit length of the model. Thus, these atoms can migrate to relatively stable positions and form low energy configurations. As G increases, the mobile atoms can move to longer distances, which explains the increase in the terrace size; Eq. (3).

The dendrite shape of maple leaf is a consequence of the particular choice of a simple cubic lattice for the model simulations. The flat terraces are the configurations of lowest energy in this lattice, which explains their relative stability. The orientations of the cation flux and of the substrate only have the effect of excluding dendrite propagation in the $-z$ direction, which is a shadowing effect.

For large G and ϵ, which is the small interaction limit (Sec. 3.2), the branches are thicker, have infrequent ramification, and propagate in the z direction. The atom mobility in the terrace borders is high. The growth direction is again related to the directions of the substrate and of the plane of cation release, but not related to the crystalline structure. Bifurcations are less frequent in the thicker branches because formation of stable configurations in other directions is difficult.

The dendrite morphology is an effect of the combination of the facile diffusion of weakly bonded atoms and the stability of low energy configurations. This stability depends on the energetics of the crystal and on the timescale in which the atoms can move at the dendrite surface. This is the time of G hop attempts in our model. Physically, this is the characteristic time of crystallization of an atomic layer, which depends on the deposition rate and, consequently, on the applied current. In the electrodeposition of a material such as silver or lead, the atoms with high mobility are those of an amorphous or polycristalline phase, respectively, as discussed in Sec. 2.3.

The formation of a secondary branch occurs when a terrace is formed in a direction which is opposite to the direction of one of the terraces of the primary branch. For instance, if the primary branch propagates in the $(1, 1, 1)$ direction, the formation of a terrace with outer normal $-y$ may lead to the formation of a secondary branch propagating in the $(1, -1, 1)$ direction. This is consistent with the energetics of the lattice structure.

Since G and ϵ are related to the temperature and to the electric current, a balance between these quantities is necessary to provide high mobility to atoms with low coordination and stability of atoms with high coordination. At very low temperature or with very high current, the atom mobility is negligible at all positions, so that the film has the disordered DLA-like features. Moreover, at high temperatures or with very small applied current, the terrace organization is destroyed.

The balance in other physical or chemical parameters to provide dendrite growth was formerly discussed by other authors. For instance, Ref. 15 analyzed the interplay of reaction rate and ion diffusivity in solution in silver electrodeposition. The balance of non-equilibrium conditions in electrodeposition of several materials was also addressed in Ref. 11, which suggested that the slower growth of flat dendrite surfaces could be a passivation effect or an effect of high mobility of atoms on those surfaces. Our model supports the second interpretation: the high mobility of atoms formed in the flat regions permits their migration to points with lower energy and, consequently, low mobility (no passivation effect is considered

in our model).

4.4 Relation to models of compact film growth

For $G \sim 10^3$ or larger, a wetting layer with very low porosity was shown to be formed on the electrode.[33] The roughness and the lateral correlation length of this layer vary in time and with distance as power laws with the same exponents of the stochastic growth equation of Villain, Lai, and Das Sarma.[51,52] Those exponents are also the same of the Clarke and Vvedensky (CV) model for solid-on-solid (non-porous) film deposition,[53] in which deposition and collective adatom diffusion take place simultaneously.

In the CV model, the atomic flux is collimated and has a rate F. The terrace diffusion coefficient has the thermally activated form

$$D = h_0 \exp\left(-E_s/k_B T\right), \tag{5}$$

where E_s is an activation energy and h_0 is a constant, and the diffusion coefficient of an atom with another neighborhood is reduced by a factor ϵ per lateral neighbor (i. e. the same factor of our electrodeposition model). The main parameter to describe the competition between these processes is the diffusion-to-deposition ratio[54,55]

$$R \equiv \frac{D}{F}, \tag{6}$$

since adatom diffusion is the mechanism that brings the system to equilibrium configurations and the flux from vapor is the mechanism that drives the system far from equilibrium.

The parameter G of the electrodeposition model has the same qualitative behavior of R as the temperature varies and as the deposition rate varies; in other words, G represents the competition between adsorbate diffusion (which is enhanced by the increase of the temperature) and the applied current (which is proportional to the deposition rate). Ref. 56 presented a simpler version of this model, in which the flux was collimated and each atom

could execute G hop attempts, but with solid-on-solid conditions (no overhangs nor pores) and with $\epsilon = 0$ (irreversible attachment to lateral neighbors). That model produces films with the same morphology of the CV model if G and R are related as

$$G \approx AR^{\nu}, \tag{7}$$

where $\nu \approx 0.6$ and A is a constant of order 10^{-1} which has a weak dependence on ϵ.[56,57] Moreover, the average size of the terraces in that model varies as $G^{1/2}$.

4.5 Consequences of the scaling of dendrite size

The qualitative relation between G and the electric current (Sec. 2.3) implies that the average dendrite size decreases as the current increases. This is observed in silver electrodeposition, in which dendrites with a feather-like morphology have tips of larger width as the current decreases.[58,59] In the electrodeposition of gold of Ref. 41, the decrease of the negative potential (which typically leads to an increase in the deposition rate) led to a change from a morphology with thick leaves to a morphology with thin dendrites. In the copper electrodeposition work of Ref. 60, as the potential decreases to more negative values and the reduction current increases, particles change from compact shape (in close to equilibrium conditions) to flower-like shape with thick leaves, then to feather-like shape with thin branches, and finally to randomly ramifying shape; this evolution is qualitatively consistent with the effect of the current predicted here.

The increase of branch size with the surface diffusivity (for constant growth rate) was predicted by a theoretical approach to instability development in electrodeposition[30] and is consistent with the increase of dendrite size with G. In Ref. 61, the study of the initial Li electrodeposition on Cu showed that lower interaction energy between the adatoms was correlated with the formation of homogeneous films, while higher energy favors dendrite growth. In this case, we understand that the lower interaction energy facilitates adsorbate

diffusion, which is consistent with our model.

However, the effect of temperature on dendrite thickness is more difficult to predict from our model. Although the temperature increase facilitates the diffusion of the adsorbate, the diffusivity in solution also increases; this may lead to an increase in the deposition rate and a decrease in the time of crystallization of an atomic layer. Depending on the relative changes of diffusivity on the surface and in solution, an increase or a decrease of the diffusion length on the surface may be observed.

Eq. (3) shows that the typical width of a dendrite is $w \sim \langle s \rangle^{1/2} \sim G^{\alpha/2}$, where $\alpha/2$ is between ≈ 0.38 and ≈ 0.43. This is the typical width of the terraces in the dendrite tips. For large G, we obtain $w \ll G^{1/2}$, which means that a terrace in a dendrite tip cannot attain the same size as a terrace attains in the growth of a compact film with the model of Ref. 56.

Despite this difference, here we propose that G is related to an effective diffusion-to-deposition ratio R as a power law, as in Eq. (7); however, we assume that the exponent ν may be different from the value 0.6 of the compact films. We will show that this assumption leads to a simple form for $\langle s \rangle$ as a function of the temperature and of the current and suggests a framework to analyze experimental data.

From Eqs. (6), (5), and (7), we have $G \sim \exp\left[-\nu E_s / \left(k_B T\right)\right] / F^{\nu}$. Assuming that the deposition rate F is proportional to the electrodeposition current I and using Eq. (3), we obtain the average dendrite thickness as

$$\langle s \rangle \sim \frac{\exp\left(-\beta E_s / k_B T\right)}{I^{\beta}} \qquad , \qquad \beta = \nu \alpha. \tag{8}$$

This relation neglects the effect of ϵ on $\langle s \rangle$ (this effect was shown to be small in Sec. 3.4).

If $\langle s \rangle$ is measured as a function of the current I, for fixed temperature, Eq. (8) predicts $\langle s \rangle \sim I^{-\beta}$; a fit of $\langle s \rangle$ versus I then gives an estimate of β. If the current is fixed and $\langle s \rangle$ is measured as a function of the temperature, an Arrhenius plot gives an estimate of the macroscopic activation energy βE_s in Eq. (8); this procedure is adopted, for example, in the

analysis of temperature dependence of lithium dendrite length in Ref. 26. The combination of these estimates provides an estimate of E_S, which is an energy barrier for diffusion on the lowest energy surfaces of the dendrites. In this procedure, note that the activation energy βE_s obtained in the Arrhenius plot is a macroscopic value which may be different from the microscopic energy barrier E_S; the correction factor β depends on the relation between size and applied current.

5 Conclusion

We performed numerical simulations of a model of thin film electrodeposition which is designed to describe effects of diffusion of the adsorbed material. This model was introduced in Ref. 33, which analyzed the growth of a wetting layer at short times and the crossover to a regime of porous film growth. Here we analyzed the film structure in this second regime and addressed the conditions for dendrite formation, which is a morphology of interest for several applications.

The conditions of low temperature or large current correspond to small values of the parameter G in our model, which leads to growth of DLA-like structures. High temperature or very small current are represented by large values of the parameters G and ϵ, in which the deposits have thick rounded columns with sporadic ramification. In these limiting cases, the average growth direction of the branches is controlled by the directions of the electrode and of the cation flux.

For $10^2 \leq G \leq 10^4$ and $\epsilon \lesssim 0.1$, the films have a hierarchical morphology with dendrites with maple leaf shape; the same morphology is also obtained with larger G, but the detachment probability ϵ has to be small. The dendrite tips are formed by three concurrent terraces and propagate in directions forming 45° with the electrode. In this regime, there are balanced conditions of adsorbate diffusion and current. The lowest energy configurations (terraces) are stable within the timescale of crystallization of an atomic layer, but weakly

bonded atoms have sufficiently large mobility to migrate to terrace borders and increase the terrace sizes. This means that the dendrite morphology and the direction of propagation are controlled by the energetics of the crystal. The particular dendrite shape obtained here is related to the choice of the simple cubic lattice structure, which facilitates the simulation of large systems. Despite this limitation, that shape is similar to those observed in electrodeposition of gold, zinc, and palladium. Moreover, the conceptual framework developed here may be useful for the analysis of dendrite formation with other shapes.

The average dendrite size was shown to increase as a power law of G and to have a small dependence on ϵ. Thus, this size is expected to decrease with the applied current, in agreement with observations in electrodeposition of silver and gold. Assuming that the adsorbate diffusion is thermally activated, we proposed that the average dendrite size is a ratio between an Arrhenius factor and a power law of the current. This result suggests a method to estimate the microscopic energy barrier of diffusion, which may be different from the activation energy obtained from Arrhenius plots of dendrite size.

A common feature of all growth conditions discussed here is the diffusive flux of cations in solution, which leads to preferential attachment at the protuberant parts of the deposit and shadowing of growth at its valleys. This is essential for the formation of branched structures, organized (dendritic) or not (DLA). Dendritic morphology may also be obtained with chemical (not electrochemical) methods in solution, as illustrated in Ref. 62. Instead, with any bias in the flux, the formation of non-fractal deposits (with finite porosity) is expected at long times, as illustrated by the model of multiparticle biased DLA;[63] see also Ref. 64 for the case of radial growth. In the extreme case of collimated flux, like in molecular beam epitaxy, compact films are formed. With techniques such as metal organic chemical vapor deposition, mixing and reactions of precursors occur as they execute a diffusive motion; however, the large mean free paths and the presence of a depletion layer near the deposit imply a partially collimated flux (although dendrites may be produced in some conditions[65,66]).

Supporting Information Available

The files animatedshortlat.avi and animatedshortside.avi have movies with lateral and top views, respectively, of growing dendrite tips, generated with $G = 10^4$ and $\epsilon = 0.05$.

This material is available free of charge via the Internet at `http://pubs.acs.org/`.

Acknowledgment

F.D.A. Aarão Reis acknowledges support from Brazilian agencies CNPq (304766/2014-3), FAPERJ (E-26/202941/2015), and CAPES (88881.068506/2014-01).

References

(1) Liu, K.; Jiang, L. Metallic surfaces with special wettability. *Nanoscale* **2011**, *3*, 825–838.

(2) Guo, F.; Su, X.; Hou, G.; Li, P. Superhydrophobic silver surface with dendrites structure on steel substrate by a facile electroless galvanic deposition process. *Appl. Surf. Sci.* **2012**, *258*, 4906–4910.

(3) Darmanin, T.; de Givenchy, E. T.; Amigoni, S.; Guittard, F. Superhydrophobic surfaces by electrochemical processes. *Adv. Mat.* **2013**, *25*, 1378–1394.

(4) Tam, J.; Palumbo, G.; Erb, U. Recent advances in superhydrophobic electrodeposits. *Materials* **2016**, *9*, 151.

(5) Wen, X.; Xie, Y. T.; Mak, W. C.; Cheung, K. Y.; Li, X. Y.; Renneberg, R.; Yang, S. Dendritic nanostructures of silver: Facile synthesis, structural characterizations, and sensing applications. *Langmuir* **2006**, *22*, 4836–4842.

(6) Rashid, M. H.; Mandal, T. K. Synthesis and catalytic application of nanostructured silver dendrites. *J. Phys. Chem. C* **2007**, *111*, 16750–16760.

(7) Yanpeng, X.; Taleb, A.; Jegou, P. Electrodeposition of cobalt films with an oriented fir tree-like morphology with adjustable wetting properties using a self-assembled gold nanoparticle modified HOPG electrode. *J. Mater. Chem. A* **2013**, *1*, 11580.

(8) Ye, W. C.; Shen, C. M.; Tian, J. F.; Wang, C. M.; Bao, L. H.; Gao, H. J. Self-assembled synthesis of SERS-active silver dendrites and photoluminescence properties of a thin porous silicon layer. *Electrochem. Comm.* **2008**, *10*, 625–629.

(9) Zhu, Y.; Zheng, H.; Yang, Q.; Pan, A.; Yang, Z.; Qian, Y. Growth of dendritic cobalt nanocrystals at room temperature. *J. Cryst. Growth* **2004**, *260*, 427–434.

(10) Sun, G.; Dong, B.; Cao, M.; Wei, B.; Hu, C. Hierarchical dendrite-like magnetic materials of Fe_3O_4, γ-Fe_2O_3, and Fe with high performance of microwave absorption. *Chem. Mater.* **2011**, *23*, 1587–1593.

(11) Fukami, K.; Nakanishi, S.; Yamasaki, H.; Tada, T.; Sonoda, K.; Kamikawa, N.; Tsuji, N.; Sakaguchi, H.; Nakato, Y. General mechanism for the synchronization of electrochemical oscillations and self-organized dendrite electrodeposition of metals with ordered 2D and 3D microstructures. *J. Phys. Chem. C* **2007**, *111*, 1150–1160.

(12) Qiu, R.; Zhang, D.; Wang, P.; Zhang, X. L.; Kang, Y. S. Tunable electrochemical preparation of cobalt micro/nanostructures and their morphology-dependent wettability property. *Electrochim. Acta* **2011**, *58*, 699–706.

(13) Qiu, R.; Zhang, D.; Wang, P. Dendritic core shell structure preparation by a facile consecutive electrochemical crystal growth method. *Electrochim. Acta* **2012**, *81*, 112–116.

(14) Nishikawa, K.; Chassaing, E.; Rosso, M. Evolution of the Morphology of Electrodeposited Copper at the Early Stage of Dendritic Growth. *J. Electrochem. Soc.* **2013**, *160*, D183–D187.

(15) Yang, T.; Liu, J.; Dai, J.; Han, Y. Shaping particles by chemical diffusion and reaction. *CrystEngComm* **2017**, *19*, 72.

(16) Witten, T. A., Jr.; Sander, L. M. Diffusion-limited aggregation, a kinetic critical phenomenon. *Phys. Rev. Lett.* **1981**, *47*, 1400–1403.

(17) Meakin, P. Diffusion-controlled deposition on fibers and surfaces. *Phys. Rev. A* **1983**, *27*, 2616–2623.

(18) Meakin, P. Diffusion-controlled deposition on surfaces: Cluster-size distribution, interface exponents, and other properties. *Phys. Rev. B* **1984**, *30*, 4207–4214.

(19) Uwaha, M.; Saito, Y. Aggregation growth in a gas of finite density: Velocity selection via fractal dimension of diffusion-limited aggregation. *Phys. Rev. A* **1989**, *40*, 4716–4723.

(20) Berkes, B. B.; Henry, J. B.; Huang, M.; Bondarenko, A. S. Electrochemical characterization of copper thin-film formation on polycrystalline platinum. *Chem. Phys. Chem.* **2012**, *13*, 3210–3217.

(21) Gründer, Y.; Markovic, N. M.; Thompson, P.; Lucas, C. A. Temperature effects on the atomic structure and kinetics in single crystal electrochemistry. *Surf. Sci.* **2015**, *631*, 123–129.

(22) Ustarroz, J.; Hammons, J. A.; Altantzis, T.; Hubin, A.; Bals, S.; Terryn, H. A generalized electrochemical aggregative growth mechanism. *J. Am. Chem. Soc.* **2013**, *135*, 11550–11561.

(23) Desai, D.; Turney, D. E.; Anantharaman, B.; Steingart, D. A.; Banerjee, S. Morphological evolution of nanocluster aggregates and single crystals in alkaline zinc electrodeposition. *J. Phys. Chem. C* **2014**, *118*, 8656–8666.

(24) Xu, S.; Zhu, Y.; Xiong, D.; Wang, L.; Yang, P.; Chu, P. K. Zinc electrodeposition on polycrystalline copper: Electrochemical study of early-stage growth mechanism. *J. Phys. Chem. C* **2017**, *121*, 3938–3946.

(25) Fang, J.; Ma, X.; Cai, H.; Song, X.; Ding, B.; Guo, Y. Double-interface growth mode of fractal silver trees within replacement reaction. *Appl. Phys. Lett.* **2006**, *89*, 173104.

(26) Aryanfar, A.; Brooks, D. J.; Colussi, A. J.; Merinov, B. V.; Goddard, W. A., III; Hoffmann, M. R. Thermal relaxation of lithium dendrites. *Phys. Chem. Chem. Phys.* **2015**, *17*, 8000–8005.

(27) Alamini, M. F.; da Silva, R. C.; Zoldan, V. C.; Isoppo, E. A.; Filho, U. P. R.; Reis, F. D. A. A.; Klein, A. N.; Pasa, A. A. Normal versus anomalous roughening in electrodeposited Prussian Blue layers. *Electrochim. Acta* **2011**, *13*, 1455.

(28) Brandt, I. S.; Zoldan, V. C.; Stenger, V.; Cid, C. C. P.; Pasa, A. A.; Oliveira, T. J.; Reis, F. D. A. A. Substrate effects and diffusion dominated roughening in Cu_2O electrodeposition. *J. Appl. Phys.* **2015**, *118*, 145303.

(29) Mahboob, S. S.; Swanson, K.; Gonzalez, J. A.; Shepherd, J. L. On the use of atomic force microscopy and scaling analysis to quantify the roughness of zinc electrodeposits produced from an industrial acid sulfate electrolyte containing glue. *J. Appl. Electrochem.* **2016**, *46*, 539–549.

(30) Aogaki, R.; Makino, T. Morphological instability in nonsteady galvanostatic electrodeposition I. Effect of surface diffusion of adatoms. *J. Electrochem. Soc.* **1984**, *131*, 40–46.

(31) Liu, J.; Liu, C.; Conway, P. P. Kinetic Monte Carlo simulation of the electrodeposition of polycrystalline copper: Effects of substrates and deposition parameters on the microstructure of deposits. *Electrochim. Acta* **2013**, *97*, 132–142.

(32) Treeratanaphitak, T.; Pritzker, M. D.; Abukhdeir, N. M. Kinetic Monte Carlo simulation of electrodeposition using the embedded-atom method. *Electrochim. Acta* **2014**, *121*, 407–414.

(33) Reis, F. D. A. A.; di Caprio, D.; Taleb, A. Crossover from compact to branched films in electrodeposition with surface diffusion. *Phys. Rev. E* **2017**, *96*, 022805.

(34) Montroll, E. W.; West, B. J. *Fluctuation phenomena*; North-Holland: Amsterdam, The Netherlands, 1979.

(35) Wang, J. *Analytical electrochemistry, 3rd ed.*; Wiley: Hoboken, NJ, USA, 2006.

(36) Fang, J.; You, H.; Kong, P.; Ding, B.; Song, X. Size-dependent structure transformation from amorphous phase to crystal. *Appl. Phys. Lett.* **2008**, *92*, 143111.

(37) Sun, M.; Liao, H.-G.; Niu, K.; Zheng, H. Structural and morphological evolution of lead dendrites during electrochemical migration. *Sci. Rep.* **2013**, *3*, 3227.

(38) Yang, T.; Han, Y. Quantitatively relating diffusion and reaction for shaping particles. *Cryst. Growth Des.* **16**, *2016*, 2850–2859.

(39) Hoshen, J.; Kopelman, R. Percolation and cluster distribution. I. Cluster multiple labeling technique and critical concentration algorithm. *Phys. Rev. B* **1976**, *14*, 3438–3445.

(40) Ye, W.; Wang, D.; Zhang, H.; Zhou, F.; Liu, W. Electrochemical growth of flowerlike gold nanoparticles on polydopamine modified ITO glass for SERS application. *Electrochim. Acta* **2010**, *55*, 2004–2009.

(41) Ye, W.; Yan, J.; Ye, Q.; Zhou, F. Template-free and direct electrochemical deposition of hierarchical dendritic gold microstructures: Growth and their multiple applications. *J. Phys. Chem. C* **2010**, *114*, 15617–15624.

(42) Monzon, L. M. A.; Klodt, L.; Coey, J. M. D. Nucleation and electrochemical growth of zinc crystals on polyaniline films. *J. Phys. Chem. C* **2012**, *116*, 18308–18317.

(43) Monzon, L. M. A.; Rode, K.; Venkatesan, M.; Coey, J. M. D. Electrosynthesis of iron, cobalt, and zinc microcrystals and magnetic enhancement of the oxygen reduction reaction. *Chem. Mater.* **2012**, *24*, 3878–3885.

(44) Liu, Z.; Cui, T.; Lu, T. Q.; Ghazvini, M. S.; Endres, F. Anion effects on the solid/ionic liquid interface and the electrodeposition of zinc. *J. Phys. Chem. C* **2016**, *120*, 20224–20231.

(45) Maniam, K. K.; Chetty, R. Electrodeposited palladium nanoflowers for electrocatalytic applications. *Fuel Cells* **2013**, *13*, 1196–1204.

(46) Kahanda, G. L. M. K. S.; Zou, X.; Farrell, R.; Wong, P. Columnar growth and kinetic roughening in electrochemical deposition. *Phys. Rev. Lett.* **1992**, *68*, 3741–3744.

(47) Pastor, J. M.; Rubio, M. A. Rough growth and morphological instability of compact electrodeposits. *Phys. Rev. Lett.* **1996**, *76*, 1848–1851.

(48) Argoul, F.; Arneodo, A.; Grasseau, G.; Swinney, H. L. Self-similarity of diffusion-limited aggregates and electrodeposition clusters. *Phys. Rev. Lett.* **1988**, *61*, 2558–2561.

(49) Schneider, N. M.; Park, J. H.; Grogan, J. M.; Steingart, D. A.; Bau, H. H.; Ross, F. M. Nanoscale evolution of interface morphology during electrodeposition. *Nature Comm.* **2017**, *8*, 2174.

(50) Krug, J. Origins of scale invariance in growth processes. *Adv. Phys.* **1997**, *46*, 139–282.

(51) Villain, J. Continuum models of crystal growth from atomic beams with and without desorption. *J. Phys. I* **1991**, *1*, 19–42.

(52) Lai, Z.-W.; Das Sarma, S. Kinetic growth with surface relaxation: Continuum versus atomistic models. *Phys. Rev. Lett.* **1991**, *66*, 2348–2351.

(53) Clarke, S.; Vvedensky, D. D. Growth kinetics and step density in reflection high-energy electron diffraction during molecular-beam epitaxy. *J. Appl. Phys.* **1988**, *63*, 2272.

(54) Ohring, M. *Materials science of thin films - deposition and structure, 2nd ed.*; Academic Press: New York, USA, 2001.

(55) Evans, J. W.; Thiel, P. A.; Bartelt, M. C. Morphological evolution during epitaxial thin film growth: Formation of 2D islands and 3D mounds. *Surf. Sci. Rep.* **2006**, *61*, 1–128.

(56) Aarão Reis, F. D. A. Dynamic scaling in thin-film growth with irreversible step-edge attachment. *Phys. Rev. E* **2010**, *81*, 041605.

(57) de Assis, T. A.; Aarão Reis, F. D. A. Dynamic scaling and temperature effects in thin film roughening. *Journal of Statistical Mechanics: Theory and Experiment* **2015**, *2015*, P06023.

(58) Liu, W.; Yang, T.; Li, C.; Che, P.; Han, Y. Regulating silver morphology via electrochemical reaction. *CrystEngComm* **2015**, *17*, 6014–6022.

(59) Che, P.; Liu, W.; Chang, X.; Wang, A.; Han, Y. Multifunctional silver film with superhydrophobic and antibacterial properties. *Nano Research* **2016**, *9*, 442–450.

(60) Gowthaman, N. S. K.; John, S. A. Fabrication of different copper nanostructures on indium-tin-oxide electrodes: shape dependent electrocatalytic activity. *CrystEngComm* **2016**, *18*, 8696–8708.

(61) Ishikawa, K.; Ito, Y.; Harada, S.; Tagawa, M.; Ujihara, T. Crystal orientation dependence of precipitate structure of electrodeposited Li metal on Cu current collectors. *Cryst. Growth Des.* **2017**, *17*, 2379–2385.

(62) Yang, T.; Han, Y.; Li, J. Manipulating silver dendritic structures via diffusion and reaction. *Chem. Eng. Sci.* **138**, *2015*, 457–464.

(63) Castro, M.; Cuerno, R.; Sanchez, A.; Dominguez-Adame, F. Multiparticle biased diffusion-limited aggregation with surface diffusion: A comprehensive model of electrodeposition. *Phys. Rev. E* **2000**, *62*, 161–173.

(64) Ferreira, S. C., Jr.; Alves, S. G.; Brito, A. F.; Moreira, J. G. Morphological transition between diffusion-limited and ballistic aggregation growth patterns. *Phys. Rev. E* **2005**, *71*, 051402.

(65) Gan, Y. X.; Hamdan, A. S.; Gan, J. B.; Li, M. Chemical vapor deposition of Bi-Te-Ni-Fe on magnesium oxide substrate and its Seebeck effect. *Coatings* **2017**, *7*, 164.

(66) Gardecka, A. J.; Bishop, C.; Lee, D.; Corby, S.; Parkin, I. P.; Kafizas, A.; Krumdieck, S. High efficiency water splitting photoanodes composed of nano-structured anatase-rutile TiO_2 heterojunctions by pulsed-pressure MOCVD. *Appl. Catal. B: Environmental* **2017**, *224*, 904–911.